0026-895X/11/8001-87–96$25.00
MOLECULAR PHARMACOLOGY
Copyright © 2011 The American Society for Pharmacology and Experimental Therapeutics
Mol Pharmacol 80:87–96, 2011

Vol. 80, No. 1
71894/3697781
Printed in U.S.A.

Structural Basis for the High-Affinity Inhibition of Mammalian Membranous Adenylyl Cyclase by 2′,3′-*O*-(*N*-Methylanthraniloyl)-Inosine 5′-Triphosphate[S]

Melanie Hübner, Anshuman Dixit, Tung-Chung Mou, Gerald H. Lushington, Cibele Pinto, Andreas Gille, Jens Geduhn, Burkhard König, Stephen R. Sprang, and Roland Seifert

Department of Pharmacology and Toxicology, University of Regensburg, Regensburg, Germany (M.H.); Molecular Modeling and Graphics Laboratory, University of Kansas, Lawrence, Kansas (A.D., G.H.L.); Center for Biomolecular Structure and Dynamics, University of Montana, Missoula, Montana (T.-C.M., S.R.S.); Department of Pharmacology and Toxicology, University of Kansas, Lawrence, Kansas (C.P., A.G.); Institute of Organic Chemistry, University of Regensburg, Regensburg, Germany (J.G., B.K.); and Institute of Pharmacology, Medical School of Hannover, Hannover, Germany (R.S.)

Received February 20, 2011; accepted April 14, 2011

ABSTRACT

2′,3′-*O*-(*N*-Methylanthraniloyl)-ITP (MANT-ITP) is the most potent inhibitor of mammalian membranous adenylyl cyclase (mAC) 5 (AC5, K_i, 1 nM) yet discovered and surpasses the potency of MANT-GTP by 55-fold (*J Pharmacol Exp Ther* **329:** 1156–1165, 2009). AC5 inhibitors may be valuable drugs for treatment of heart failure. The aim of this study was to elucidate the structural basis for the high-affinity inhibition of mAC by MANT-ITP. MANT-ITP was a considerably more potent inhibitor of the purified catalytic domains VC1 and IIC2 of mAC than MANT-GTP (K_i, 0.7 versus 18 nM). Moreover, there was considerably more efficient fluorescence resonance energy transfer between Trp1020 of IIC2 and the MANT group of MANT-ITP compared with MANT-GTP, indicating optimal interaction of the MANT group of MANT-ITP with the hydrophobic pocket. The crystal structure of MANT-ITP in complex with the $G_s\alpha$- and forskolin-activated catalytic domains VC1:IIC2 compared with the existing MANT-GTP crystal structure revealed only subtle differences in binding mode. The higher affinity of MANT-ITP to mAC compared with MANT-GTP is probably due to fewer stereochemical constraints upon the nucleotide base in the purine binding pocket, allowing a stronger interaction with the hydrophobic regions of IIC2 domain, as assessed by fluorescence spectroscopy. Stronger interaction is also achieved in the phosphate-binding site. The triphosphate group of MANT-ITP exhibits better metal coordination than the triphosphate group of MANT-GTP, as confirmed by molecular dynamics simulations. Collectively, the subtle differences in ligand structure have profound effects on affinity for mAC.

Introduction

Mammals express nine membranous AC isoforms (ACs 1–9) that play an important role in transmembrane signal transduction (Sunahara et al., 1996; Tang and Hurley, 1998). ACs are activated by the G-protein G_s via numerous receptors for hormones and neurotransmitters and catalyze the production of the second-messenger cAMP. Studies with AC5(−/−) mice indicate that potent and selective AC5 inhibitors may be valuable drugs for the treatment of heart failure, aging, bone loss, anxiety, and acute and chronic pain (Chester and Watts, 2007; Rottlaender et al., 2007; Kim et al., 2008; Okumura et al., 2009).

Previous studies from our group showed that 2′,3′-*O*-(*N*-methylanthraniloyl) (MANT)-substituted purine nucleotides are competitive AC inhibitors and inhibit AC isoforms differentially (Gille and Seifert, 2003; Gille et al., 2004). Moreover, MANT nucleotides are fluorescence probes of conformational changes in the catalytic site of AC. Crystal structures of the purified catalytic subunits of $G_s\alpha$-bound mammalian AC [C1 subunit of AC5 (VC1) and C2 subunit of AC2 (IIC2) in complex with MANT-GTP and MANT-ATP] were resolved (Mou

This work was supported by the National Institutes of Health National Institute of Diabetes and Digestive and Kidney Diseases [Grant DK46371] (to S.R.S); the Deutsche Forschungsgemeinschaft [Grant Se 529/5–2] (to R.S.); and the Elite Network of Bavaria (graduate research scholarship to M.H.).

Article, publication date, and citation information can be found at http://molpharm.aspetjournals.org.

doi:10.1124/mol.111.071894.

[S] The online version of this article (available at http://molpharm.aspetjournals.org) contains supplemental material.

ABBREVIATIONS: AC, adenylyl cyclase; MANT, 2′,3′-*O*-(*N*-methylanthraniloyl); FS, forskolin; GTPγS, guanosine 5′-[γ-thio]triphosphate; MES, 2-(*N*-morpholino)ethanesulfonic acid; PDB, Protein Data Bank; GBSA, Generalized Born, augmented by solvent-accessible surface; FRET, fluorescence resonance energy transfer; λ_{ex}, excitation wavelength; λ_{em}, emission wavelength; mAC, mammalian membranous adenylyl cyclase; VCI and IIC2, the N- and C-terminal catalytic domains, respectively, from canine AC5 and rat AC2 expressed as soluble proteins.

et al., 2005, 2006). Those studies revealed a tripartite binding pocket for MANT nucleotides in the catalytic core consisting of sites for the base, the MANT-substituted ribosyl group, and the polyphosphate chain. The combined analysis of enzymatic, fluorescence spectroscopy, crystallographic, and molecular modeling data revealed that the MANT group contributes most to the AC binding energy, whereas the base makes the smallest contribution. This is reflected by the fact that MANT nucleotides exhibit up to 17,000-fold higher affinity for AC than their nonsubstituted parent nucleotides and that purine and pyrimidine nucleotides exhibit similar affinity for AC (Gille et al., 2004, 2005). On the basis of those data, we proposed that ACs exhibit a high degree of conformational flexibility, allowing the catalytic site to accommodate structurally diverse bases (Mou et al., 2006; Wang et al., 2007).

During the course of our subsequent systematic studies on 2′,3′-*O*-ribosyl-substituted nucleotides as mAC inhibitors (Göttle et al., 2009; Suryanarayana et al., 2009), we serendipitously identified MANT-ITP as the most potent mAC inhibitor known so far. Specifically, MANT-ITP inhibits AC5 with a K_i value of 1 nM and mouse heart AC (predominantly representing AC5) with a K_i value of 4 nM. Compared with MANT-GTP, MANT-ITP possesses a 55-fold higher affinity for recombinant AC5. The base hypoxanthine differs chemically from the base guanine by the absence of an NH_2 group at C2 of the purine ring (Fig. 1). Accordingly, hypoxanthine cannot to form a hydrogen bond with the backbone oxygen of Ile1019 (Mou et al., 2005). On the basis of analogous studies with GTP, ITP, and XTP on GTP-binding proteins (Seifert et al., 1999; Gille et al., 2003; Gille and Seifert, 2004), one would also expect that the missing hydrogen bond should actually reduce affinity of mAC for MANT-ITP. This notion is further supported by the fact that MANT-XTP, bearing a keto group at C2 of the purine ring (Fig. 1), binds to mAC with much lower affinity than MANT-GTP because of electrostatic repulsion of the keto group of the xanthine group by the backbone oxygen of Ile1019 (Mou et al., 2005).

Therefore, the aim of our present study was to elucidate the structural basis for the high-affinity interaction of mAC with MANT-ITP, using the VC1:IIC2 heterodimer as an established model of the mAC catalytic domain. First, we determined the affinities of VC1:IIC2 for MANT-GTP, MANT-ITP, and MANT-XTP in enzyme activity assays (Gille et al., 2004). Second, we performed fluorescence studies with the three MANT nucleotides (Mou et al., 2006). Third, we analyzed the crystal structure of VC1:IIC2 in complex with MANT-ITP and compared this structure with the known VC1:IIC2 structure in complex with MANT-GTP (Mou et al., 2005). Last, we conducted molecular dynamics simulations to further evaluate the structural requirements for the high-affinity interaction of MANT-ITP with AC5 in comparison to MANT-GTP (Wang et al., 2007). Here, we show that even subtle differences in ligand structure have profound effects for interaction with mAC.

Materials and Methods

Materials. MANT-ITP was synthesized according to Hiratsuka (1983) with the modifications described by Taha et al. (2009). MANT-GTP and MANT-XTP were obtained from Jena Bioscience (Jena, Germany). [α-^{32}P]ATP (800 Ci/mmol) was purchased from PerkinElmer Life and Analytical Sciences (Boston, MA). Aluminum oxide 90 active, neutral (activity 1, particle size 0.06–0.2 mm) was purchased from Merck (Darmstadt, Germany). Bovine serum albumin, fraction V, highest quality, was from Sigma-Aldrich (St. Louis, MO). $MnCl_2$ tetrahydrate (highest quality) was from Merck. FS was from LC Laboratories (Woburn, MA).

AC Activity Assay. AC activity was determined essentially as described in the literature (Mou et al., 2005). In brief, reaction mixtures contained 100 μM ATP/Mn^{2+}, 10 mM $MnCl_2$, and MANT

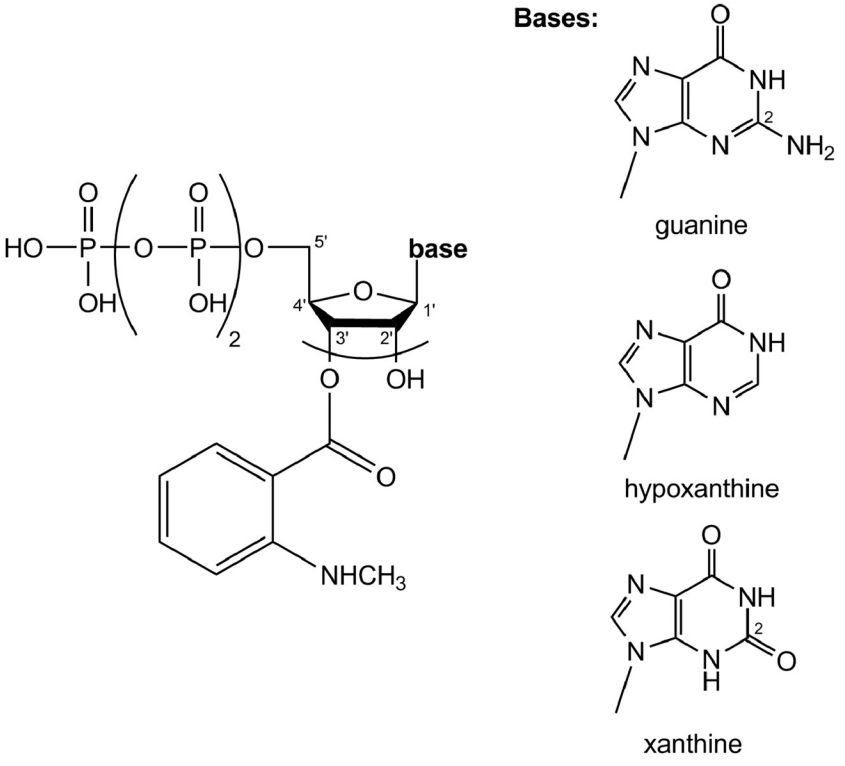

Fig. 1. Structure of MANT nucleoside 5′-triphosphates (NTPs). Represented are MANT-ITP, MANT-GTP, and MANT-XTP, the MANT nucleotides used for enzymatic studies, fluorescence spectroscopy, crystallography, and structure activity evaluation. The MANT group isomerizes between the 2′ and 3′-*O*-ribosyl function. Note the different substitution of the C2 carbon atom of the purine ring in the various nucleotides.

nucleotides at concentrations from 0.1 nM to 1 mM as appropriate to obtain saturated inhibition curves. In addition, assay tubes contained VC1 (8 nM) and IIC2 (40 nM). For experiments with $G_s\alpha$-GTPγS, tubes contained VCI (3 nM), IIC2 (15 nM) and $G_s\alpha$-GTPγS (51 nM). Reactions were conducted in the presence of 100 μM FS. After a 2-min preincubation at 30°C, reactions were initiated by adding 20 μl of reaction mixture containing (final) 1.0 μCi/tube [α-^{32}P]ATP, 0.1 mM cAMP, and 100 mM KCl in 25 mM HEPES/NaOH, pH 7.4. Reactions were conducted for 10–20 min at 30°C and were terminated by the addition of 20 μl of 2.2 N HCl. Denatured protein was precipitated by a 1-min centrifugation at 25°C and 15,000*g*. Sixty-five microliters of the supernatant fluid were applied onto disposable columns filled with 1.3 g of neutral alumina. [^{32}P]cAMP was separated from [α-^{32}P]ATP by elution of [^{32}P]cAMP with 4 ml of 0.1 M ammonium acetate, pH 7.0. Recovery of [^{32}P]cAMP was ~80% as assessed with [^{3}H]cAMP as standard. [^{32}P]cAMP was determined by liquid scintillation counting using Ecolume scintillation cocktail (Thermo Fisher Scientific, Waltham, MA). Competition isotherms were analyzed by nonlinear regression using the Prism 4.0 software (GraphPad Software, San Diego, CA).

Fluorescence Spectroscopy. All experiments were conducted using a Cary Eclipse fluorescence spectrophotometer equipped with a Peltier-thermostated multicell holder at 25°C (Varian, Palo Alto, CA). Measurements were performed in a quartz fluorescence microcuvette (Hellma, Plainview, NY). The final assay volume was 150 μl. Reaction mixtures contained a buffer consisting of 100 mM KCl, 10 mM $MnCl_2$, and 25 mM HEPES/NaOH, pH 7.4. Steady-state emission spectra were recorded at low speed with λ_{ex} = 350 nm (λ_{em} = 370–500 nm) and λ_{ex} = 280 nm (λ_{em} = 300–500 nm) with various MANT nucleotides (1 μM each) in the absence and presence of 5 μM VC1 plus 25 μM IIC2 without and with 100 μM FS. Fluorescence recordings were analyzed with the spectrum package of the Cary Eclipse software (Varian, Walnut Creek, CA). Baseline fluorescence (buffer alone) was subtracted. Figure 2 shows superimposed original fluorescence recordings representative for two to three independent experiments with at least two different batches of VC1:IIC2.

Preparation of Proteins. The catalytic subunits VC1, IIC2, and GTPγS-activated $G_s\alpha$ were expressed in *Escherichia coli* BL21(DE3) cells containing pREP4 plasmid. The plasmids encode the wild-type C1a domain of canine AC 5 (residues 364–580), the C2a domain of rat AC 2 (residues 874-1018), and bovine $G_s\alpha$ (residues 1–396). VC1 and $G_s\alpha$ constructs were expressed with a hexahistidine tag at their N- and C-termini, respectively. They were purified and stored as described previously (Tesmer et al., 2002). $G_s\alpha$ was further activated by incubation with 500 μM GTPγS and 2 mM $MgCl_2$ at 30°C for 2 h, and digestion of the complex with trypsin was necessary for crystallization work. The smaller fragment, containing residues 39–387 was further purified using a nickel-nitrilotriacetic acid-NTA column followed by MonoQ anion exchange chromatography.

Complex Formation and Crystallization with MANT-ITP. To form a stable heterotrimeric complex, the recombinant proteins were mixed in the following order VC1-IIC2–$G_s\alpha$–GTPγS in a molar ratio 1.5:1:1. Thereafter, forskolin (200 μM) was added to further stabilize the complex. The protein mixture was incubated on ice for at least 30 min and then applied to tandem-arranged Superdex 75 and 200 gel filtration columns (GE Healthcare, Chalfont St. Giles, Buckinghamshire, UK). Only the fractions containing the complex were collected and concentrated to ~9.5 mg/ml in a buffer of 20 mM HEPES, pH 8.0, 1 mM EDTA, 2 mM $MgCl_2$, 5 mM dithiothreitol, 100 mM NaCl, 200 μM 7-acetyl-7-[O-(*N*-methylpiperazino)-γ-butyryl)]-forskolin, and 500 μM GTPγS. The concentrated protein solution was used to grow crystals via the sitting-drop method with a reservoir solution of 7.2% (m/v) polyethylene glycol 8000, 0.5 M NaCl, and 0.1 M MES, pH 5.4, at 16°C for 3 to 4 weeks. Large crystals were soaked with 2 mM MANT-ITP and 3 mM $MnCl_2$ for at least 2 h at room temperature and then harvested in a cryoprotectant consisting of 9% (m/v) polyethylene glycol 8000, 30% (m/v) polyethylene glycol 400, 0.1 M MES, pH 5.4, 0.5 M NaCl, 20 mM HEPES, pH 8.0, 1 mM EDTA, 2 mM dithiothreitol, 200 μM 7-acetyl-7-[O-(*N*-methyl-piperazino)-γ-butyryl)]-forskolin, 100 μM GTPγS, 2 mM MANT-ITP, and 3 mM $MnCl_2$. The cryoprotected crystals were mounted in 0.1- to 0.2-mm loops and stored in liquid nitrogen.

Structure Determination and Model Refinement. Diffraction data sets were collected at the Stanford Synchrotron Radiation Lightsource SSRL-SMB-MC 9-1 beamline (Stanford, CA) by the oscillation method (1°/frame, 60 s/frame). The incident beam wavelength was 0.9795 Å. The images were processed using the HKL2000 package (Otwinowski and Minor, 1997). Because of anisotropy of the plate-type crystal, data with *l* index >21 were excluded from the data set. Structures were determined by molecular replacement using the structure of the $G_s\alpha$-GTPγS:VC1:IIC2 complex [Protein Data Bank (PDB) code 1AZS] as the initial phasing model (Tesmer et al., 1997). Atomic positions and thermal parameters of the mAC structure were refined by Refmac5.5 using the CCP4 program suite (Collaborative Computational Project Number 4, 1994). MANT-ITP and metal ions in the structure were located in the weighted $|F_o| - |F_c|$ omit map computed with phases from the refined model. The model was iteratively improved by manual refitting into weighted $2|F_o| - |F_c|$ map using the computer graphics program Coot (Emsley and Cowtan, 2004) and subsequent refinement cycles with CCP4. The refined crystal structure was visualized with PyMOL (DeLano, 2002). Coordinates for the MANT-ITP:Mn^{2+} structure were deposited in the Protein Data Bank with the code PDB 3G82.

Molecular Dynamics Simulations. Atomic coordinates of protein-ligand complexes for MANT-ITP and MANT-GTP interacting with VC1:IIC2 were extracted from structures PDB 3G82 and PDB 1TL7. Ligand parametrization for FS, MANT-GTP, and MANT-ITP was performed by extracting the relevant ligands from the crystal structures and editing them via SYBYL (Tripos Inc., St. Louis, MO) to ensure proper representation of valence and bond types. Thereafter, the antechamber (Wang et al., 2001) module of AMBER10 (http://www.ambermd.org) was used to assign Austin model 1-bond charge correction (AM1-BCC) charges to the ligands and calculate force field parameters for them. To avoid excessively large computational expense, only the VC1:IIC2 portion of each crystal structure (plus ligand and cofactor) was retained; bound $G_s\alpha$-GTPγS was removed. The tleap module of AMBER10 was used for the preparation of topology and coordinate files for the protein-ligand complexes using the ff99SB force field parameters for protein and the antechamber-calculated parameters for ligands. The parameters for Mn^{2+} were obtained from Bradbrook et al. (1998). The structures PDB 3G82 and PDB 1TL7 were separately solvated in water boxes with buffering distance of 10 Å. Assuming normal charge states of ionizable groups corresponding to pH 7.0, Na^+ ions were added to achieve charge neutrality and to mimic the biological environment more closely.

Our primary simulation engine for probing the differences in the dynamic nature of the two complexes was NAMD (Phillips et al., 2005; http://www.ks.uiuc.edu/Research/namd/), which was chosen because of its excellent parallel scalability, which enabled us to perform the simulations in an expeditious manner on 32 nodes of a large Linux cluster. To relieve severe steric contacts and instances of higher energy conformations that might destabilize the molecular dynamics integrator at later stages, the system was subjected to initial minimization of 2×10^4 steps wherein the protein backbone was held fixed (to relax surrounding water molecules and computationally specified hydrogen positions), followed by 2×10^4 steps of minimization without positional constraints (i.e., to allow the system to relax freely). The resulting low-energy (~0 K) model was then equilibrated to room temperature (~300 K) by gradually increasing the system temperature in increments of 20 K up to a target temperature of 300 K. At each of the 15 temperature increments, 1.5×10^4 dynamics steps (30 ps) were run while employing a restraint of 10 kcal · mol^{-1} · Å^{-2} on protein α carbons (C_α) to avoid any prospect of unrealistic denaturation behavior. Thereafter, the system was equilibrated for 15×10^4 steps (300 ps) at 310 K (approximate

physiological temperature) under conditions of constant volume and temperature, and then for a further 15×10^4 steps (300 ps) at 310 K using a Langevin piston (constant pressure and temperature) to achieve uniform pressure of 1 bar. Finally the restraints were removed and the system was equilibrated for 5×10^6 steps (1 ns) to prepare the system for final analysis. For the latter, a constant pressure and temperature simulation was run on the equilibrated structure for 9.6 ns, keeping the temperature at 310 K and pressure at 1 bar using Langevin piston coupling algorithm. The integration time step of the simulations was set to 2.0 fs, the SHAKE algorithm was used to constrain the lengths of all chemical bonds involving hydrogen atoms at their equilibrium values, and the geometry was restrained rigidly via the SETTLE algorithm. Nonbonded van der Waals interactions were treated via a switching function at 10 Å and reaching zero influence at a distance of 12 Å, and the Mn^{2+} cofactors were subjected to a soft harmonic constraint (1 kcal/mol) to encourage adherence to equilibrium approach distances relative to the ligand phosphate oxygens as determined from an earlier simulation. The particle-mesh Ewald algorithm as implied in NAMD was used to handle long-range electrostatic forces.

To probe relative contributions to the total free energy of the complexes, we employed the GBSA (Generalized Born, augmented by solvent-accessible surface) method (Weiser et al., 1999; Bashford and Case, 2000; Onufriev et al., 2000). For this, the trajectory obtained from the molecular dynamics run was converted into individual coordinate files at 100-ps intervals excluding the initial 1.0 ns of the simulation. Thus, 86 frames were used in GBSA calculation for each complex. AMBER parameters (using bonding radii for GBSA calculation) were then generated from the resulting structures using tleap and were subsequently applied in GBSA calculation. The radii for

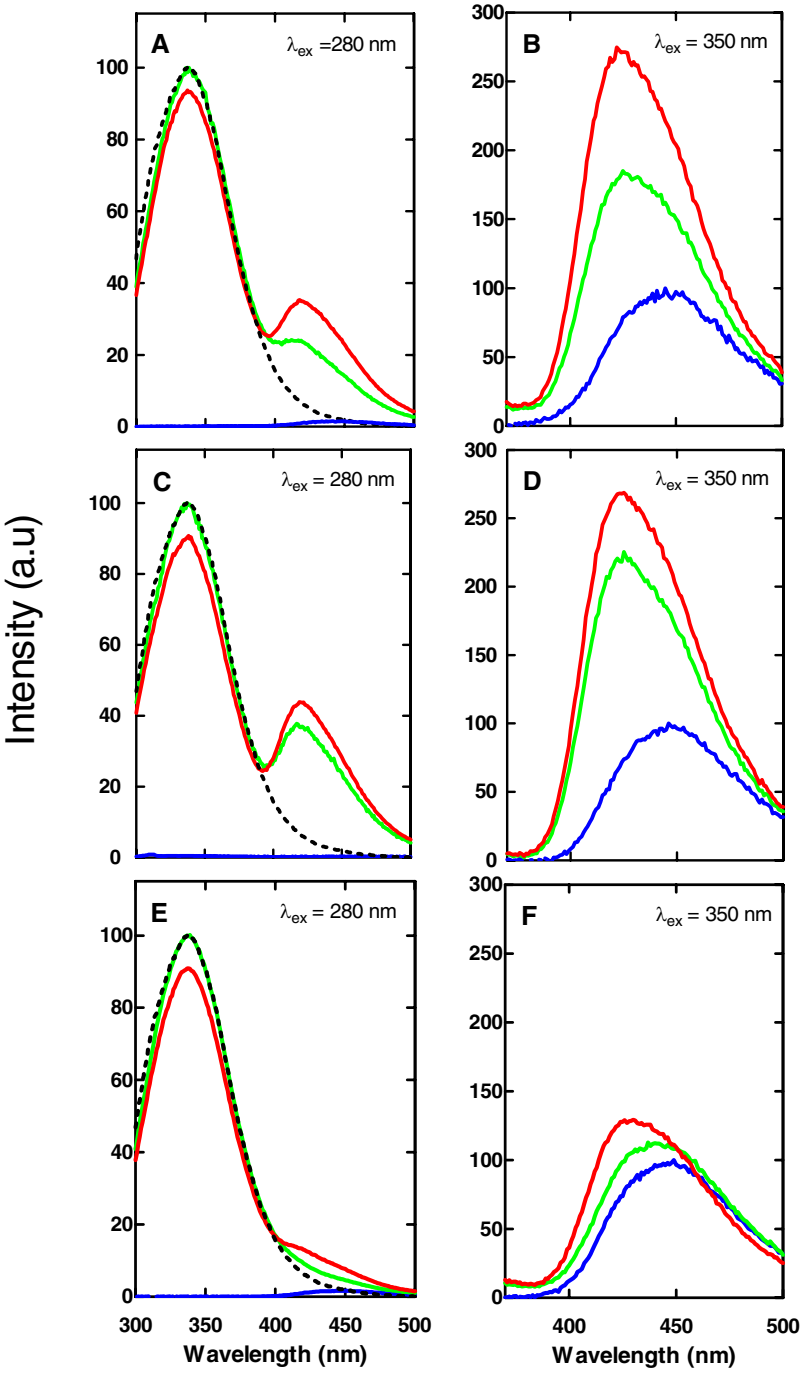

Fig. 2. Fluorescence emission spectra of MANT-GTP, MANT-ITP and MANT-XTP. Emission at λ_{ex} = 280 nm (λ_{em} = 300–500 nm) and at λ_{ex} = 350 nm (λ_{em} = 370–500 nm) are represented. Experiments were conducted at 25°C. Addition of MANT nucleotides (1 μM), blue lines; subsequent addition of VC1 (5 μM) and IIC2 (25 μM), green lines; subsequent addition of FS (100 μM), red lines. Dashed lines in A to C represent endogenous tyrosine/tryptophan fluorescence of VC1:IIC2. Reaction mixtures contained a buffer of 100 mM KCl, 10 mM $MnCl_2$, and 25 mM HEPES/NaOH, pH 7.4. Three independent experiments with at least two different batches of VC1:IIC2 were performed. A and B, MANT-GTP; C and D, MANT-ITP; E and F, MANT-XTP. Fluorescence intensities are shown in arbitrary units (a.u.). For FRET (A, C, and E, λ_{ex} = 280 nm), the fluorescence observed with VC1:IIC2 was set to 100%. In direct fluorescence experiments (B, D, and F, λ_{ex} = 350 nm), the fluorescence observed with MANT nucleotides alone was set to 100%.

Mn^{2+} was specified as being the same as Mg^{2+}, because GBSA parameters for Mn^{2+} are unavailable in AMBER. The change of conformational entropy was not considered. Apart from a number of settings chosen specifically for this analysis, default GBSA parameters were employed [implicit Generalized Born (IGB) = 2 to specify the Onufriev, Bashford and Case (OBC) model, GBSA = 1 to choose the linear combination of pairwise overlaps (LCPO) method for solvent-accessible surface area calculation, external dielectric (EXTDIEL) = 78.50 to set the solvent dielectric for room-temperature water, internal dielectric (INTDIEL) = 1.0 to specify a solute dielectric for the system, and surface tension (SURFTEN) = 0.0072 to describe the water surface tension].

Results

Enzymatic Studies. Table 1 lists the K_i values of MANT-GTP, MANT-ITP, and MANT-XTP for inhibition of VC1:IIC2 under maximally stimulatory conditions (i.e., in the presence of $G_s\alpha$-GTPγS) as well as under submaximally stimulatory conditions (i.e., in the absence of $G_s\alpha$-GTPγS). The latter reflects the assay conditions for the fluorescence spectroscopy studies. In accordance with the data for AC5 and mouse heart AC (Göttle et al., 2009), under maximally stimulatory conditions, MANT-ITP was a considerably more potent inhibitor of VC1:IIC2 than MANT-GTP, which, in turn, was much more potent than MANT-XTP. The omission of $G_s\alpha$-GTPγS reduced the overall MANT nucleotide potencies by 4- to 10-fold, but the rank order of affinity of nucleotides was preserved. Collectively, the enzyme inhibition studies with purified catalytic subunits of mAC confirmed the exceptionally high affinity of MANT-ITP for the catalytic site previously reported for AC5 and mouse heart AC (Göttle et al., 2009).

Fluorescence Spectroscopy Studies. To elucidate further differences in the interaction of MANT nucleotides with VC1:IIC2, we exploited the fluorescence properties of these nucleotides (Jameson and Eccleston, 1997) and the ability of the MANT group to bind to a hydrophobic pocket in the interface of VC1:IIC2 (Mou et al., 2005, 2006). The emission spectra of nucleotides at λ_{ex} = 350 nm for direct excitation of the MANT group (Jameson and Eccleston, 1997), and at λ_{ex} = 280 nm for analysis of FRET between Trp1020 in IIC2 and the MANT group were determined (Mou et al., 2005). Fluorescence studies were performed in the presence of a 5-fold excess of VC1 relative to MANT nucleotides to ensure quantitative ligand binding to the catalytic site.

TABLE 1

Inhibitory potencies of MANT-NTPs on the catalytic activity of VC1:IIC2

Catalytic activities of VC1:IIC2 were determined as described under *Materials and Methods*. Reactions were conducted in the presence of 10 mM $MnCl_2$ and 100 μM FS in the absence or presence of $G_s\alpha$-GTPγS. Data were analyzed by nonlinear regression to calculate K_i values. The catalytic activity of C1/C2 in the presence of Mn^{2+} + FS + $G_s\alpha$-GTPγS with 100 μM ATP as substrate was 2700 ± 350 nmol · mg^{-1} · min^{-1} and in the presence of Mn^{2+} + FS, the activity was 300 ± 110 nmol · mg^{-1} · min^{-1}. The K_m values for VC1:IIC2 were reported previously (Mou et al., 2005) for each experimental condition (430 and 620 μM, respectively) and were used to calculate K_i values from IC_{50} values. Data are the mean values ± S.D. of two to four independent experiments performed in duplicates with at least two different batches of protein.

MANT-Nucleotide	K_i VC1:IIC2 Mn^{2+}	
	+ FS + $G_s\alpha$-GTPγS	+ FS
	nM	
MANT-GTP	18 ± 6.0	130 ± 20
MANT-ITP	0.7 ± 0.1	7.0 ± 3.2
MANT-XTP	1,200 ± 370	4,600 ± 510

At λ_{ex} = 280 nm, MANT nucleotides were only minimally excited, whereas at λ_{ex} = 350 nm, they showed substantial intrinsic fluorescence signals with an emission peak at ~450 nm (Fig. 2, blue tracings). The dashed black lines indicate the endogenous tryptophan fluorescence of VC1:IIC2 at λ_{ex} = 280 nm (i.e., the fluorescence in the absence of MANT nucleotide). After the addition of VC1:IIC2, at λ_{ex} = 280 nm, MANT-ITP exhibited a much higher basal FRET signal, as revealed by a second emission peak at λ_{em} = 420 nm, than MANT-GTP (Fig. 2, A and C, green tracings). At λ_{ex} = 350 nm, the interaction of MANT-ITP with VC1:IIC2 resulted in considerably higher increases in fluorescence compared with MANT-GTP (Fig. 2, B and D, green tracings). The blue shift of the fluorescence emission (Mou et al., 2005) was similar for MANT-ITP and MANT-GTP. FS (100 μM) increased basal FRET and direct fluorescence with MANT-GTP more effectively than with MANT-ITP, but the absolute FRET with MANT-ITP was still considerably larger than with MANT-GTP. These data suggest that the MANT group of MANT-ITP binds to the hydrophobic pocket in mAC more effectively than MANT-GTP. Compared with MANT-GTP and MANT-ITP, MANT-XTP exhibited only minimal FRET and direct fluorescence (Fig. 2, E and F), reflecting suboptimal binding of the xanthine ring to mAC and suboptimal insertion of the MANT group into the hydrophobic pocket (Mou et al., 2005).

Crystallographic Studies. To better understand the high inhibitory potency of MANT-ITP at ACs 1, 2, and 5 (Göttle et al., 2009), as well as at the catalytic domains VC1:IIC2 (Table 1), crystallographic studies were conducted. Crystals of FS-VC1:IIC2-$G_s\alpha$-GTPγS were soaked with 2 mM MANT-ITP and 3 mM $MnCl_2$. The structure of the MANT-ITP:Mn^{2+} complex was determined at a resolution of 3.1 Å by molecular replacement using the structure of the $G_s\alpha$-GTPγS:VC1:IIC2 complex as the initial phasing model (Tesmer et al., 1997) (PDB code 1AZS). Crystallographic data collection and refinement statistics are summarized in Table 2. Interactions between $G_s\alpha$-GTPγS and the pseudosymmetric VC1 and IIC2 catalytic domains center largely on IIC2, as described previously (Tesmer et al., 1997). The two domains form a very large interface, facilitating the binding of MANT-ITP at the catalytic site, and FS at the pseudo–dyad-related site. The structure was very similar to the corresponding complex with MANT-GTP (Fig. 1) (Mou et al., 2005) (PDB code 1TL7). Superimposing the two structures revealed that the overall placement of VC1 and IIC2 did not differ greatly from each other with the root-mean-square deviation less than 0.5 Å (Fig. 3C).

MANT-ITP was modeled into the continuous $|F_o|-|F_c|$ map in the binding pocket. The electron density was more consistent with 3′-*O*-MANT-ITP than the 2′-*O*-MANT isomer (Fig. 3A). Our previous crystallographic studies with MANT-GTP and MANT-ATP gave similar results (Mou et al., 2005; 200). Difference electron density peaks corresponding to the two Mn^{2+} ions are observed; wherein the A site exhibits lower occupancy than the B site, suggesting that the Mn^{2+} ion is bound more tightly at the B site, as observed in other mAC crystal structures (Mou et al., 2005, 2006).

The overall conformation of MANT-ITP bound to VC1:IIC2 is similar to that observed for MANT-GTP. The ligands are similar with respect to interactions with protein residues and metal ion coordination (Fig. 3, B and D). The $|F_o|-|F_c|$ electron density for MANT-ITP is well defined and similar to

that observed for MANT-GTP, indicating no obvious difference in the conformation of the two ligands. One noticeable difference is that the hypoxanthine ring of MANT-ITP lacks an amino group at the C2 position (Fig. 1) that could form a hydrogen bond with the side chain of Ile1019 of IIC2 domain (MANT-GTP 2.6 Å; Fig. 3D). Despite the absence of this interaction, MANT-ITP binds with higher affinity to VC1:IIC2 than MANT-GTP, as indicated above (Table 1). The absence of the C2-amino group allows a higher degree of mobility of the purine moiety than in the case of MANT-GTP (Fig. 3D). The purine ring of MANT-ITP is somewhat more deeply inserted in the mAC binding site than that of MANT-GTP.

In the crystal structure, the MANT group of MANT-ITP and MANT-GTP form similar interactions at the $\alpha 4'$-$\alpha 1$ domain interface. The aryl function of MANT engages in hydrophobic interactions with Ala409, Leu412, Val413, Val1024, Val1026, and Trp1020 (Fig. 4). The increase in the fluorescence signal for MANT-ITP may be due to changes of the relative positions of Trp1020 and the MANT group (Fig. 2). However, electron density is weak for the MANT moiety, suggesting that it is poorly ordered within the binding site (Fig. 3A). The oxygen of the carbonyl group of MANT-ITP is closer to Asn1025 than that of MANT-GTP (Fig. 4). However, in this orientation, the side chain of Asn1025 does not form an H-bond with the carbonyl group of MANT-ITP.

A stronger interaction of MANT-ITP with the phosphate binding site is supported by two observations. The side chain Lys1065 of IIC2 interacts with the β- and γ-phosphates of MANT-ITP, whereas the amino group of Lys1065 in the MANT-GTP structure is oriented only toward the γ-phosphate (Fig. 3C). The amino group of Lys1065 is also closer to the oxygen of the β-phosphate of MANT-ITP (2.9 Å) compared with the oxygen of the γ-phosphate of MANT-GTP (3.1 Å).

TABLE 2
Summary of crystallography data collection and refinement statistics

Parameters	MANT-ITP:Mn^{2+}
Cell constants (Å)	
a	117.6
b	133.4
c	70.6
No. of crystals	1
D_{min} (Å)	3.1
Average redundancy	3.0 (1.8)[a]
R_{sym} (%)[b]	17.9 (34.5)
Completeness (%)	81.4 (55.1)
$<I>/<\sigma>$	4.5 (1.7)
Resolution range for refinement (Å)[c]	15–3.1
Total reflections used	15824
No. of protein atoms	5645
No. water molecules	5
No. ligand atoms	106
rmsd bond length (Å)	0.007
rmsd bond angle (°)	1.21
R_{work} (%)[d]	24.1
R_{free} (%)[e]	29.4
Average B-factor (Å^2)	45.2

rmsd, root mean square deviation.
[a] Numbers in parentheses correspond to the statistical data from the highest resolution shell.
[b] $R_{sym} = \Sigma_h \Sigma_i \mid I(h) - I(h)_i \mid / \Sigma_h \Sigma_i I(h)_i$, where $I(h)$ is the mean intensity after rejections.
[c] Because of anisotropy, data with an *l* index greater than 21 were omitted from refinement.
[d] $R_{work} = \Sigma_h \mid\mid F_o(h) \mid - \mid F_c(h) \mid\mid / \Sigma_h \mid F_o(h) \mid$, $F_o(h)$ and $F_c(h)$ are the observed and calculated structure factors, respectively.
[e] 5.1% of the complete data set was excluded from refinement to calculate R_{free}.

Of particular interest are the differences between the MANT-ITP and MANT-GTP complexes with respect to coordination of the Mn^{2+} ions by the nucleotide β and γ phosphates and the side chain of Asp396. The carboxylate group of Asp396 coordinates the two metal ions, together with the nucleotide phosphates and Ile397 and Asp440 of VC1 (Fig. 3B). Diffuse electron density in the region of the β-phosphate is consistent with conformational heterogeneity of the ligand and, consequently, its ligation of the Mn^{2+} ions at the A and B sites (Fig. 3A). This may account in part for differences in metal coordination for MANT-ITP and MANT-GTP. The Mn^{2+} ions in the MANT-ITP structure form close contacts with the α- and γ-phosphates, whereas in the MANT-GTP structure, the Mn^{2+} ions interact predominantly with the β-phosphate. The β-phosphate group of MANT-ITP also seems to be more tightly coordinated, because of the shorter (2.8 Å) contact with the carbonyl group of Ile397, than is the case for MANT-GTP (3.4 Å). The phosphate site plays a crucial role for binding affinity because phosphate group removal dramatically reduces inhibitor potency (Gille et al., 2004).

Molecular Dynamics Simulations. Our molecular dynamics simulations corroborate the finding that MANT-ITP has affinity for VC1:IIC2 higher than that of MANT-GTP. Specifically, the GBSA free energy analysis determined a total free energy for the MANT-ITP/VC1:IIC2 system of -99.71 ± 10.29 kcal/mol (mean ± S.D., as derived from sampling 86 time steps), whereas the MANT-GTP/VC1:IIC2 system complex had a free energy of only -69.60 ± 8.94 kcal/mol. Nearly all of this difference can be accounted for in terms of two factors: the NT-ITP complex was predicted to derive a substantial advantage from electrostatics (-951.66 ± 36.75 versus -847.41 ± 38.66 kcal/mol for MANT-GTP) but to incur a penalty in terms of a less favorable solvation profile (890.24 ± 30.79 versus 819.68 ± 34.53 kcal/mol). To ascertain the source of these interaction differences, we performed distance analysis over a set of ~9600 sample conformers (taken from each 1000 time steps in the 9.6-ns simulation) to identify any specific receptor-ligand interatomic distances that differed significantly from one ligand to the other. The most important distinction was found not in comparing the hypoxanthine and guanine rings (the only true chemical difference between the two ligands), but rather in the interactions between the Mn^{2+} ions of the receptor and an oxygen on the β-phosphate group of the ligand triphosphate moiety. Specifically, although both ligands orient one α-, one β-, and one γ-phosphate oxygen in close association to one or more of the metal ions, the dynamic conformation of MANT-ITP enables a second β oxygen to remain significantly closer to a Mn^{2+} ion (2.36 ± 0.08 Å) than is the case for MANT-GTP (3.29 ± 0.65 Å). The substantially shorter mean distance between the MANT-ITP β oxygen and the nearest Mn^{2+} suggests a significantly stronger electrostatic interaction (Fig. 5). Specifically, a twist in the orientation of the nucleobase propagates through the ribosyl moiety (in ways that do not substantially affect the interactions of these groups) to the triphosphate chain. The triphosphate group is pulled approximately 0.7 Å closer to the nucleobase, which has the important effect of positioning both β oxygens of MANT-ITP (rather than just one for MANT-GTP) in an orientation that permits interaction with Mn^{2+} ions. It is noteworthy that the much greater S.D.

observed for the β oxygen to Mn^{2+} interaction in MANT-GTP complex suggests that the manganese ion can interact more readily with solvent in the latter case, which is a plausible cause for the more favorable solvation energy for the MANT-GTP complex. Supplemental Fig. 1 and Supplemental Tables 1 to 3 provide further details on the differences in interactions of MANT-GTP and MANT-IP with VC1:IIC2.

Discussion

We developed a tripartite pharmacophore model for mAC with a binding site for the base, the (substituted) ribosyl group, and the polyphosphate chain (Mou et al., 2005, 2006). In a previous study, we reported that MANT-GTPγS and MANT-inosine 5′-[γ-thio]triphosphate are similarly potent inhibitors of various mACs (Gille et al., 2004). Omission of the MANT group reduces inhibitor affinity by several orders of magnitude, highlighting the importance of the MANT-binding site for high inhibitor affinity (Gille et al., 2004). It is noteworthy that unsubstituted inosine 5′-[γ-thio]triphosphate is a more potent mAC inhibitor than GTPγS, whereas GTP and ITP exhibit similar affinity (Gille et al., 2005). In contrast, MANT-ITP is a considerably more potent mAC inhibitor than MANT-GTP (Göttle et al., 2009). These data indicate that subtle structural changes in nucleotide inhibitors (exchange guanine and hypoxanthine; exchange γ-phosphate and γ-thiophosphate) substantially change the relative contributions of the three binding subsites in mAC for inhib-

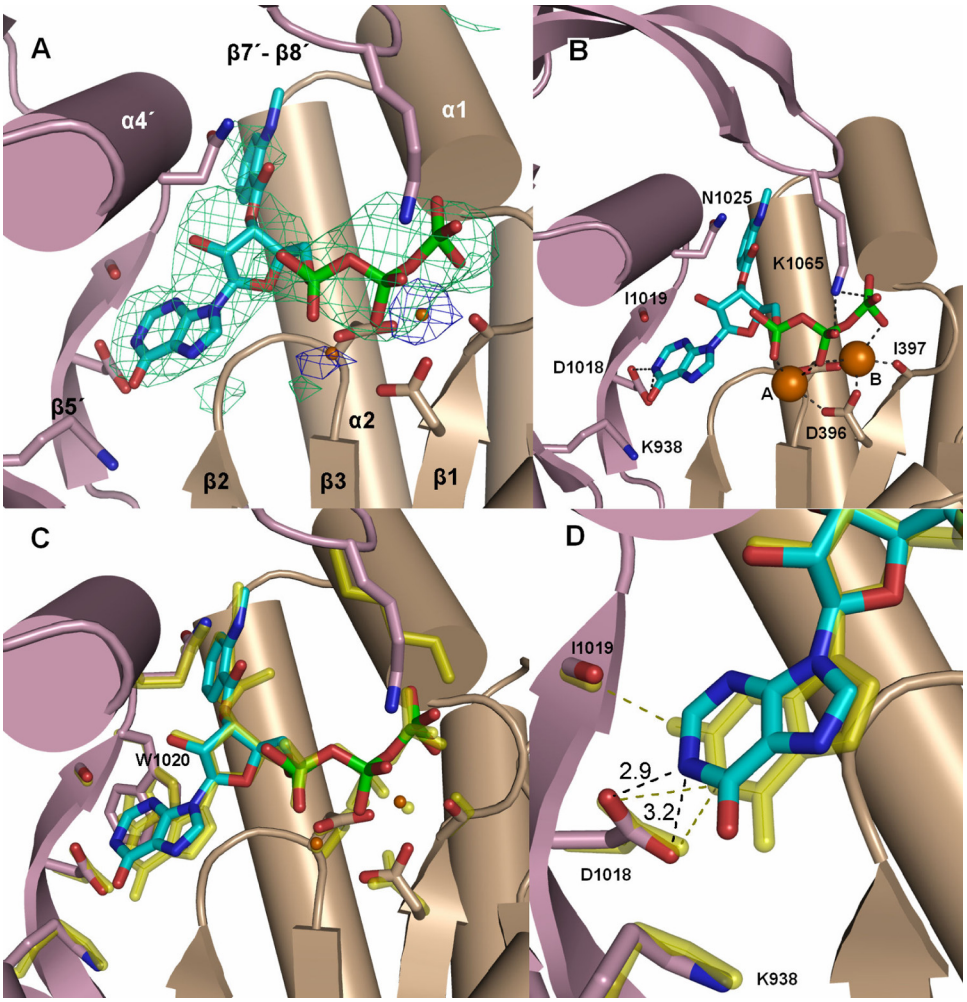

Fig. 3. Binding mode of MANT-ITP and two Mn^{2+} ions in the catalytic site. MANT-ITP and two metal ions are bound in the cleft between the soluble C1a and C2a domains. VC1 and IIC2 are colored wheat and light pink, respectively. MANT-ITP is shown as stick model, carbon atoms are cyan, nitrogen atoms are dark blue, oxygen atoms are red, and phosphorus atoms are green. The two Mn^{2+} ions are shown as orange spheres. A, difference electron density for 3′-*O*-MANT-ITP and Mn^{2+}. The lime green wire represents the $|F_o|-|F_c|$ electron density for MANT-ITP contoured at 2.5 σ. The *blue* wire corresponds to the $|F_o|-|F_c|$ electron density for the two Mn^{2+} ions contoured at 5 σ. The coordinates for the ligands were omitted from the phasing model. The secondary structure elements of the complex are labeled as defined previously (Tesmer et al., 1997). B, detailed view of substrate binding site of VC1:IIC2 with MANT-ITP:Mn^{2+}. The catalytic site of VC1:IIC2 shows MANT-ITP, A- and B- site of two Mn^{2+} ions and the protein residues that are responsible for ligand interaction. The interaction among protein residues and MANT-ITP, Mn^{2+} are shown as dashed gray lines. C, superimposed crystal structures of 3′-*O*-MANT-ITP and 3′-O-MANT-GTP. The derived MANT-ITP crystal structure was superimposed and compared with the crystal structure of MANT-GTP, shown as a transparent yellow stick model (Protein Data Bank code 1TL7) (Mou et al., 2005). The protein residues are in almost identical conformation, and the inhibitors are situated in the substrate binding pocket in a similar fashion. D, superimposed purine binding site of 3′-*O*-MANT-ITP and 3′-O-MANT-GTP. The interaction of the hypoxanthine ring and guanine ring of MANT-ITP and MANT-GTP are shown as dashed black and olive green lines, respectively. The distances of hydrogen bond between the hypoxanthine ring and surrounding protein residues of MANT-ITP are indicated in Ångstroms. The hydrogen bond between Ile1019 and the amino group of MANT-GTP is missing in the MANT-ITP structure. Lys938 and the oxygen of the hypoxanthine ring are further apart. The hypoxanthine ring has less binding constraint in the purine binding pocket in comparison to the guanine ring of MANT-GTP.

itor affinity. The main goal of the present study was to elucidate the structural basis for the exceptionally high affinity of mAC for MANT-ITP (Göttle et al., 2009).

Our data suggest that a balance of binding energies among the three pharmacophores in the mAC binding site (Mou et al., 2006) considerably affects the affinity of mAC for MANT-ITP versus MANT-GTP. The MANT-ITP structure shares the common features with previously published mAC structures in complex with 2′,3′-substituted purine and pyrimidine nucleotide inhibitors, where the base, triphosphate, and 2′,3′-ribose substituents reside in three distinct grooves of the substrate binding site (Mou et al., 2005, 2006). The overall conformations of MANT-ITP and MANT-GTP show only minimal differences. This result is not surprising. The crystal structures were derived with a racemic mixture of 2′-*O*- and 3′-*O*-MANT-ITP. Both structures favor the 3′-*O*-MANT isomer for binding to the catalytic center as shown with the MANT-GTP and MANT-ATP crystals (Mou et al., 2005, 2006).

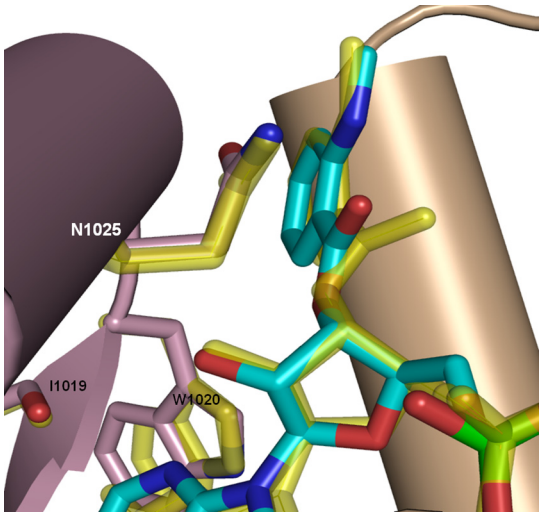

Fig. 4. MANT-binding site. A detailed view of the MANT-binding site is depicted. MANT-ITP is shown as a stick model; carbon atoms are cyan, nitrogen atoms are dark blue, oxygen atoms are red and one phosphorus atom is displayed in green. VC1 and IIC2 are colored wheat and light pink, respectively. MANT-GTP is shown as a transparent yellow stick model. The carbonyl group of MANT-ITP is in closer contact to Asn1025 but does not interact with the side chain of Asn1025 in this orientation. Apart from this, no conformational differences between MANT-ITP and MANT-GTP are detected. However, MANT-ITP might exert stronger hydrophobic interactions due to changes of the relative positions of Trp1020 and the MANT group.

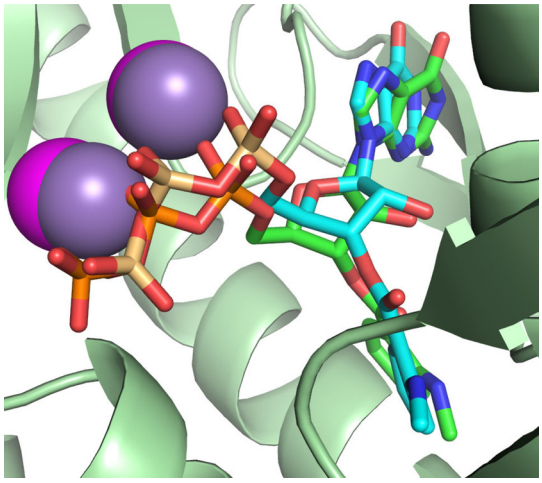

Fig. 5. Comparison of the binding of MANT-ITP and MANT-GTP by molecular dynamics simulations. Overlaid graphical representations of the terminal (t = 9.6 ns) time steps for the MANT-GTP (CPK-colored sticks with green carbons and orange phosphorus atoms) and MANT-ITP (CPK-colored sticks with cyan carbons and tan phosphorus atoms) interacting with the VC1:IIC2 receptor (pale green ribbons) and its cofactor Mn^{2+} ions (magenta spheres for MANT-GTP simulation and purple for MANT-ITP). Additional details on differences in the interactions of MANT-GTP and MANT-ITP with VC1:IIC2 are provided in Supplemental Fig. 1 and Supplemental Tables 1 to 3.

A very intriguing finding was the subtle difference in binding mode of MANT-ITP versus MANT-GTP at the purine-binding site in comparison with the exceptionally high inhibitory potency of the nucleotide. Usually, high inhibitory potency is accomplished through strong binding of the inhibitor to the active site of the enzyme. In this case, there were actually fewer protein-ligand interactions because of a missing hydrogen bond in hypoxanthine compared with guanine (Figs. 1 and 3D). However, a gain in affinity is related not only to the number of hydrogen bonds but also to hydrophobic interactions, residual mobility of the ligand, and partial solvation of the binding pocket (Gohlke and Klebe, 2002). The loss of hydrogen bonds does not necessarily lead to a decrease in binding affinity of a ligand to a protein as assessed by molecular thermodynamic and crystallographic studies of thermolysin inhibitors (Morgan et al., 1991). Binding of those inhibitors is dependent not only on hydrogen bonding but also on metal coordination and higher ligand basicity (Grobelny et al., 1989). For binding of MANT-ITP, the absence of the C(2) amino group eliminates a potential hydrogen bond but at the same time reduces spatial constraints at the purine binding site, thereby allowing other protein-nucleotide interactions to be optimized. Our crystallographic studies and molecular dynamics simulations clearly show that positioning of the β-oxygen of the triphosphate chain of MANT-ITP allows for more favorable interactions with Mn^{2+} than the triphosphate chain of MANT-GTP, providing a straightforward explanation for the observed difference in affinity (Figs. 3 and 5).

Direct fluorescence experiments and FRET studies detected stronger hydrophobic interaction of the MANT group of MANT-ITP with the hydrophobic pocket compared with that of MANT-GTP (Fig. 2). In contrast, binding of MANT-XTP does not result in an increase in direct fluorescence or FRET. Compared with MANT-ITP and MANT-GTP, MANT-XTP is at least 60-fold less potent at VC1:IIC2 (Table 1). MANT-XTP bears an oxygen at the C2-position of the purine ring (Fig. 1) that interacts unfavorably with Asp1018 in the base-binding pocket. This may move the MANT group away from the hydrophobic pocket, leading to a strong decrease in inhibitory potency and fluorescence emission. As suggested for metal-phosphate interactions, alleviation of binding constraints at the purine-binding pocket may allow MANT-ITP to form more favorable nonpolar interactions with the MANT binding site than is possible for MANT-GTP, resulting in larger fluorescence signals.

MANT-ITP is the most potent competitive inhibitor of membranous ACs known so far (Table 1) (Göttle et al., 2009). MANT-ITP is most useful as fluorescence probe for biophysical (Fig. 2) and crystallographic studies (Figs. 3 and 4) to obtain detailed molecular information on ligand/receptor interactions. Another application of MANT-ITP is to use this

ligand in screening programs for the development of AC inhibitors, avoiding the use of the classic radioactive AC assay with [α-^{32}P]ATP as substrate. Specifically, upon binding to the substrate-binding site, nonfluorescent inhibitors would quench the large basal or FS-stimulated direct fluorescence or FRET signals. This assay is even feasible to obtain information on relative inhibitor affinity through the analysis of cumulative concentration/quench curves in a single cuvette (Geduhn et al., 2011). Fluorescence assays with MANT-ITP could also be useful to identify allosteric AC inhibitors.

However, the usefulness of MANT-ITP per se as starting point for the development of AC isoform-specific inhibitors, particularly AC5 inhibitors for the treatment of heart failure, aging, bone loss, anxiety, and acute and chronic pain (Chester and Watts, 2007; Rottlaender et al., 2007; Kim et al., 2008; Okumura et al., 2009) is limited for several reasons. First, MANT-ITP per se is membrane-impermeant and would have to be delivered as a prodrug (Laux et al., 2004; Hübner et al., 2011). Second, the selectivity of MANT-ITP for AC5 relative to other AC isoforms is only very moderate (Göttle et al., 2009), because the catalytic site of the membranous AC isoforms is highly conserved (Mou et al., 2005). Third, one should also keep in mind that hypoxanthine-based nucleotides bind not only to mACs but also to other signal-transducing proteins, including soluble guanylyl cyclase and G-proteins (Seifert et al., 1999; Gille et al., 2003, 2004, 2005; Hübner et al., 2011). Accordingly, pleiotropic effects unrelated to direct mAC inhibition could arise (Hübner et al., 2011). Despite these reservations regarding MANT-ITP, the long-term goal of obtaining isoform-specific AC inhibitors is not elusive. Specifically, we have shown that certain bis-MANT-substituted nucleotides are very potent inhibitors of the *Bordetella pertussis* AC toxin CyaA (Geduhn et al., 2011), with high selectivity relative to mammalian ACs. The identification of Bis-MANT nucleotides as potent and selective CyaA inhibitors resulted from a relatively small medicinal chemistry program and not from an extensive high-throughput screening effort. Unfortunately, Bis-MANT nucleotides are not very potent inhibitors of mACs because the catalytic site of these ACs is not spacious enough.

In conclusion, our data confirm the three-site pharmacophore model already postulated in previous studies (Mou et al., 2005, 2006). Our data also show that small differences in ligand structure can have a profound impact on interactions with mAC. The one missing opportunity for hydrogen bonding in MANT-ITP relative to MANT-GTP enhances mobility of the ligand in the catalytic site, thereby facilitating hydrophobic interactions of the MANT group with surrounding amino acids and optimal positioning of the triphosphate chain to divalent cations. Together, these factors result in exceptionally high-affinity binding of MANT-ITP for mAC.

Acknowledgments

We thank the staff at the Stanford Synchrotron Radiation Lightsource SMB-MC 9-1 beamline (Stanford, CA) for their assistance with data collection. Thanks are also due to the reviewers for a helpful critique that stimulated us to resolve the mAC:MANT-ITP crystal structure and to conduct molecular dynamics simulations.

Authorship Contributions

Participated in research design: Hübner, Dixit, Mou, Lushington, Pinto, Gille, Geduhn, König, Sprang, and Seifert.

Conducted experiments: Hübner, Mou, Pinto, Gille, and Seifert.

Contributed new reagents or analytic tools: Geduhn and König.

Performed data analysis: Hübner, Dixit, Mou, Lushington, Pinto, Gille, Geduhn, Sprang, and Seifert.

Wrote or contributed to the writing of the manuscript: Hübner, Dixit, Mou, Lushington, Pinto, Gille, Geduhn, König, Sprang, and Seifert.

References

Bashford D and Case DA (2000) Generalized Born models of macromolecular solvation effects. *Annu Rev Phys Chem* **51:**129–152.

Bradbrook GM, Gleichmann T, Harrop SJ, Habash J, Raftery J, Kalb J, Yariv J, Hillier IH, and Helliwell JR (1998) X-ray and molecular dynamics studies of concanavalin-A glucoside and mannoside complexes relating structure to thermodynamics of binding. *J Chem Soc Faraday Trans* **94:**1603–1611.

Chester JA and Watts VJ (2007) Adenylyl cyclase 5: a new clue in the search for the "fountain of youth"? *Sci STKE* **413:**pe64.

Collaborative Computational Project Number 4 (1994) The CCP4 suite: programs for protein crystallography. *Acta Crystallogr D Biol Crystallogr* **50:**760–763.

DeLano WL (2002) The PyMOL Molecular Graphics System, DeLano Scientific, San Carlos, CA.

Emsley P and Cowtan K (2004) Coot: model-building tools for molecular graphics. *Acta Crystallogr D Biol Crystallogr* **60:**2126–2132.

Geduhn J, Dove S, Shen Y, Tang WJ, König B, and Seifert R (2011) Bis-halogen-anthraniloyl-substituted nucleoside 5′-triphosphates as potent and selective inhibitors of *Bordetella pertussis* adenylyl cyclase toxin. *J Pharmacol Exp Ther* **336:**104–115.

Gille A, Wenzel-Seifert K, Doughty MB, and Seifert R (2003) GDP affinity and order state of the catalytic site are critical for function of xanthine nucleotide-selective G_{α}s proteins. *J Biol Chem* **278:**7822–7828.

Gille A, Lushington GH, Mou TC, Doughty MB, Johnson RA, and Seifert R (2004) Differential inhibition of adenylyl cyclase isoforms and soluble guanylyl cyclase by purine and pyrimidine nucleotides. *J Biol Chem* **279:**19955–19969.

Gille A, Guo J, Mou TC, Doughty MB, Lushington GH, and Seifert R (2005) Differential interactions of G-proteins and adenylyl cyclase with nucleoside 5′-triphosphates, nucleoside 5′-[γ-thio]triphosphates and nucleoside 5′-[β,γ-imido]triphosphates. *Biochem Pharmacol* **71:**89–97.

Gille A and Seifert R (2003) 2′(3′)-*O*-(*N*-methylanthraniloyl)-substituted GTP analogs: a novel class of potent competitive adenylyl cyclase inhibitors. *J Biol Chem* **278:**12672–12679.

Gille A and Seifert R (2004) Xanthine nucleotide-specific G-protein α-subunits: a novel approach for the analysis of G-protein-mediated signal transduction. *Naunyn Schmiedebergs Arch Pharmacol* **369:**141–150.

Göttle M, Geduhn J, König B, Gille A, Höcherl K, and Seifert R (2009) Characterization of mouse heart adenylyl cyclase. *J Pharmacol Exp Ther* **329:**1156–1165.

Gohlke H and Klebe G (2002) Approaches to the description and prediction of the binding affinity of small-molecule ligands to macromolecular receptors. *Angew Chem Int Ed Engl* **41:**2644–2676.

Grobelny D, Goli UB, and Galardy RE (1989) Binding energetics of phosphorus-containing inhibitors of thermolysin. *Biochemistry* **28:**4948–4951.

Hiratsuka T (1983) New ribose-modified fluorescent analogs of adenine and guanine nucleotides available as substrates for various enzymes. *Biochim Biophys Acta* **742:**496–508.

Hübner M, Dizayee S, Matthes J, Seifert R, and Herzig S (2011) Effect of MANT-nucleotides on L-type calcium currents in murine cardiomyocytes. *Naunyn Schmiedebergs Arch Pharmacol*. doi:10.1007/s00210-011-0626-x.

Jameson DM and Eccleston JF (1997) Fluorescent nucleotide analogs: synthesis and applications. *Methods Enzymol* **278:**363–390.

Kim KS, Lee KW, Baek IS, Lim CM, Krishnan V, Lee JK, Nestler EJ, and Han PL (2008) Adenylyl cyclase-5 activity in the nucleus accumbens regulates anxiety-related behavior. *J Neurochem* **107:**105–115.

Laux WH, Pande P, Shoshani I, Gao J, Boudou-Vivet V, Gosselin G, and Johnson RA (2004) Pro-nucleotide inhibitors of adenylyl cyclases in intact cells. *J Biol Chem* **279:**13317–13332.

Morgan BP, Scholtz JM, Ballinger MD, Zipkin ID, and Bartlett PA (1991) Differential binding energy: a detailed evaluation of the influence of hydrogen-bonding and hydrophobic groups on the inhibition of thermolysin by phosphorus-containing inhibitors. *J Am Chem Soc* **113:**297–307.

Mou TC, Gille A, Fancy DA, Seifert R, and Sprang SR (2005) Structural basis for the inhibition of mammalian membrane adenylyl cyclase by 2′(3′)-*O*-(*N*-methylanthraniloyl)-guanosine 5′-triphosphate. *J Biol Chem* **280:**7253–7261.

Mou TC, Gille A, Suryanarayana S, Richter M, Seifert R, and Sprang SR (2006) Broad specificity of mammalian adenylyl cyclase for interaction with 2′,3′-substituted purine- and pyrimidine nucleotide inhibitors. *Mol Pharmacol* **70:**878–886.

Okumura S, Suzuki S, and Ishikawa Y (2009) New aspects for the treatment of cardiac diseases based on the diversity of functional controls on cardiac muscles: effects of targeted disruption of the type 5 adenylyl cyclase gene. *J Pharmacol Sci* **109:**354–359.

Onufriev A, Bashford D, and Case DA (2000) A modification of the generalized Born model suitable for macromolecules. *J Phys Chem B* **104:**3712–3720.

Otwinowski Z and Minor W (1997) Processing of X-ray diffraction data collected in oscillation mode. *Methods Enzymol* **276:**307–326.

Phillips JC, Braun R, Wang W, Gumbart J, Tajkhorshid E, Villa E, Chipot C, Skeel RD, Kalé L, and Schulten K (2005) Scalable molecular dynamics with NAMD. *J Comput Chem* **26:**1781–1802.

Rottlaender D, Matthes J, Vatner SF, Seifert R, and Herzig S (2007) Functional adenylyl cyclase inhibition in murine cardiomyocytes by 2′(3′)-*O*-(*N*-methylanthraniloyl)-guanosine 5′-[γ-thio]triphosphate. *J Pharmacol Exp Ther* **321:**608–615.

Seifert R, Gether U, Wenzel-Seifert K, and Kobilka BK (1999) Effects of guanine, inosine, and xanthine nucleotides on β_2-adrenergic receptor/G_s interactions: evidence for multiple receptor conformations. *Mol Pharmacol* **56:**348–358.

Sunahara RK, Dessauer CW, and Gilman AG (1996) Complexity and diversity of mammalian adenylyl cyclases. *Annu Rev Pharmacol Toxicol* **36:**461–480.

Suryanarayana S, Göttle M, Hübner M, Gille A, Mou TC, Sprang SR, Richter M, and Seifert R (2009) Differential inhibition of various adenylyl cyclase isoforms and soluble guanylyl cyclase by 2′,3′-*O*-(2,4,6-trinitrophenyl)-substituted nucleoside 5′-triphosphates. *J Pharmacol Exp Ther* **330:**687–695.

Taha HM, Schmidt J, Göttle M, Suryanarayana S, Shen Y, Tang WJ, Gille A, Geduhn J, König B, Dove S, et al. (2009) Molecular analysis of the interaction of anthrax adenylyl cyclase toxin, edema factor, with 2′(3′)-*O*-(*N*-methyl)anthraniloyl-substituted purine and pyrimidine nucleotides. *Mol Pharmacol* **75:**693–703.

Tang WJ and Hurley JH (1998) Catalytic mechanism and regulation of mammalian adenylyl cyclases. *Mol Pharmacol* **54:**231–240.

Tesmer JJ, Sunahara RK, Fancy DA, Gilman AG, and Sprang SR (2002) Crystallization of complex between soluble domains of adenylyl cyclase and activated $G_s\alpha$. *Methods Enzymol* **345:**198–206.

Tesmer JJ, Sunahara RK, Gilman AG, and Sprang SR (1997) Crystal structure of the catalytic domains of adenylyl cyclase in a complex with $G_s\alpha$.GTPγS. *Science* **278:**1907–1916.

Wang JL, Guo JX, Zhang QY, Wu JJ, Seifert R, and Lushington GH (2007) A conformational transition in the adenylyl cyclase catalytic site yields different binding modes for ribosyl-modified and unmodified nucleotide inhibitors. *Bioorg Med Chem* **15:**2993–3002.

Wang JM, Wang W, and Kollman PA (2001) ANTECHAMBER: an accessory software package for molecular mechanical calculations. *J Mol Graph* **8:**52–56.

Weiser J, Shenkin PS, and Still WC (1999) Approximate atomic surfaces from linear combinations of pairwise overlaps (LCPO). *J Comp Chem* **20:**217–230.

Address correspondence to: Dr. Roland Seifert, Institute for Pharmacology, Medical School of Hannover, Carl-Neuberg-Strasse 1, D-30625 Hannover, Germany. E-mail: seifert.roland@mh-hannover.de